

Closed-loop wavefront calibration of a multi-electrode electrowetting-based tunable microlens

Daniel Sauter^{✉*} and Hans Zappe[✉]

University of Freiburg, Laboratory for Micro-optics, Department of Microsystems Engineering—IMTEK, Freiburg, Germany

ABSTRACT. Tunable liquid micro-optical lenses and phase shifters based on multi-electrode electrowetting actuation are often subject to wavefront errors due to processing irregularities or surface defects. To enable the correction of these anomalies, we present here a method that allows calibration and compensation for wavefront errors, thereby leading to the best possible optimization of the tunable optical surface. The approach relies on a measurement of the transmitted wavefront using a Shack–Hartmann sensor and subsequent determination of the actual surface shape. The deviation between this and the target surface shape is calculated, and the electrode voltages are iteratively adjusted. A decentralized control algorithm is implemented which treats the meniscus height at each electrode as a variable with independent feedback; an adaptive update condition determines which electrodes should be adjusted in each cycle. Experimentally obtained calibration curves for a 32-electrode device demonstrate the power and utility of the method.

© The Authors. Published by SPIE under a Creative Commons Attribution 4.0 International License. Distribution or reproduction of this work in whole or in part requires full attribution of the original publication, including its DOI. [DOI: [10.1117/1.JOM.5.1.014003](https://doi.org/10.1117/1.JOM.5.1.014003)]

Keywords: liquid lens; electrowetting; calibration; closed-loop; control

Paper 24018G received Jul. 30, 2024; revised Oct. 23, 2024; accepted Dec. 16, 2024; published Jan. 16, 2025.

1 Introduction

Tunable liquid microlenses based on electrowetting actuation have undergone considerable development and seen a significant increase in functionality over the past several decades. Starting from simple, focus-tunable lenses,¹ the technology has advanced to produce lenses with tunable asphericity,² beam steering devices,³ lenses with integrated tunable apertures,⁴ or tunable cylindrical lenses.⁵ Recent applications of such devices include underwater hyperspectral imaging,⁶ depth estimation,⁷ and continuous zoom systems.⁸

Especially interesting in this area are designs with a large number of electrodes as they offer a greater degree of shape control, enabling the generation of astigmatic or higher-order deformable surfaces.^{9,10} In addition, by varying the control voltages, their function can be dynamically reprogrammed to act as a lens, a prism, or both.^{11,12} Nevertheless, like all electrowetting lenses, their liquid interface is affected by irregularities of the electrode dielectric and surface coating that may arise during manufacturing or assembly. However, the high electrode density allows local defects to be compensated by adjusting the voltage in the affected area; for example, electrodes with a thicker dielectric layer will require higher voltages. Thus, manufacturing anomalies can be compensated if the effect of the error can be determined.

*Address all correspondence to Daniel Sauter, Daniel.Sauter@imtek.uni-freiburg.de

One compensation approach is to monitor the current and thus indirectly the capacitance of each electrode during operation.¹³ Before using the device in an application, the covered area of each electrode is related to a measured current. Generation of a specific surface shape is then a matter of controlling the voltages until the corresponding current is reached. Although this method is very effective, a large number of measurement channels are needed for devices with high electrode counts such as the ones we will discuss here. An alternative approach is by directly optimizing the output of the device using optical feedback. In the case of an electrowetting laser scanner, this was demonstrated by comparing the position of a deflected laser beam to a grid target and iteratively adjusting the voltages to minimize errors.¹⁴

We demonstrate here that the same principle of output optimization can be applied to lenses by analyzing the transmitted wavefront. The difference between target and reconstructed surface shapes is minimized by stepwise adjustment of electrode voltages. To achieve this, a control structure is used which assigns a single control term to each electrode and dynamically selects which electrodes are updated.¹⁵

Conceptually, our approach combines aspects of both iterative learning and decentralized control. Similarly to decentralized control, the complex control problem is subdivided into manageable subproblems, in this case by looking at each electrode individually.¹⁶ The process of repeating actuation cycles with different inputs to optimize the output is an essential aspect of iterative learning control.¹⁷

The voltage data obtained in this calibration process may then be used to operate the lens. Although the method is applicable to all electrowetting lenses, we demonstrate its effectiveness here using a cylindrical device that employs electrodes embedded in a polymer foil positioned on the inner circumference of a fluidic tube for actuation.

2 Microlens Structure

A schematic diagram of the lens structure is given in Fig. 1(a). It consists of a cylindrical glass cavity that is filled with two immiscible liquids with differing refractive index. Refraction occurs at the interface between the liquids whose curvature can be controlled through electrowetting on dielectrics. As a result, the focal length of the lens changes with the applied voltage. The electrode area consists of 32 individually addressable segments which enable the creation of astigmatic surfaces such as the one shown in Fig. 1(b).

The key element is the polymer foil that sits on the inner sidewall of the liquid cavity. It contains the electrode segments and their electrical connections, as well as the functional hydrophobic surface coating to achieve a large initial contact angle. The liquid inside the cavity is sealed by microstructured glass substrates on either side of the tube, which also acts as an aperture. The iridium oxide aperture on the bottom also acts as the electrical connection for the lens liquid.

The lens is driven by a 40-channel high-voltage amplifier (OKO Tech, Rijswijk, Netherlands) via a custom interfacing circuit board that accepts the flex connectors of the foil

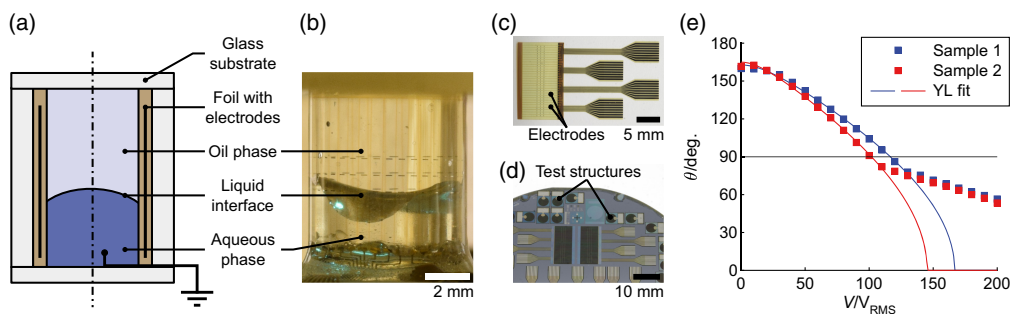


Fig. 1 (a) Schematic showing a cross-section of the microlens and its structure. (b) Side view of an operational lens with a toroidally shaped liquid interface. The transparent electrodes are visible slightly as vertical lines. (c) Polymer foil that contains the electrodes before insertion into the tube. (d) Test structures located on the same wafer to characterize the fabricated foils. (e) Measured contact angle curves of two samples from the same fabrication run.

[shown in Fig. 1(c)]. To avoid charge trapping, 1-kHz sinusoidal signals are used for actuation. Tuning of individual electrodes is then accomplished by modulating the amplitude of the sine on the respective channel. The water-based liquid mixture OHGL and OHZB serves as the active lens fluid with a refractive index of $n_{\text{OHGL}+\text{OHZB}} = 1.519$. The ambient liquid is laser liquid 433 with $n_{433} = 1.293$ (all liquids are sourced from Cargille Laboratories, Cedar Grove, New Jersey, United States; n given at 589.3 nm and 25°C). Both liquids inside the tube are density-matched to negate gravity effects.

Fabrication of the polymer foil is done using standard microstructuring processes. First, a polyimide base layer is spun onto a handle wafer. Then, the transparent indium tin oxide electrodes and platinum conductive paths are sputter-deposited and structured in a lift-off step. Subsequently, another polyimide layer is spun onto the wafer, followed by a hydrophobic Cytop layer, which gives the surface a high initial contact angle of 160 deg. Figure 1(c) shows a foil that has been removed from the wafer and is ready to be inserted into the tube.

As the electrowetting characteristics depend on the dielectric thickness and surface quality of the coating, variations are to be expected between fabrication runs and wafers. To characterize the foils, contact angle test structures are included on the wafer which undergo the same fabrication steps and should therefore have identical electrowetting characteristics. Figure 1(d) shows such test structures in close proximity to the foils. They have a circular electrode area with a diameter of 4 mm. The contact angle curves are measured by submersing the structure in ambient liquid, dispensing a 2- μL droplet onto the electrode area, and applying a varying voltage to this droplet with respect to the electrode. The changing contact angle is recorded using a goniometer (OCA15Pro, DataPhysics Instruments GmbH, Filderstadt, Germany).

In severe cases, the measured behavior can differ significantly among samples located on the same wafer as exemplified in Fig. 1(e). The data show the averaged contact angle values for multiple actuation cycles and their respective fit of the Young–Lippman equation (labeled “YL fit”). Deviations of this kind are caused by either variations in coating thickness or, less likely, inhomogeneities in the dielectric properties.

Further defects can arise during the handling of the foil and assembly of the lens (further information about assembly and filling in Refs. 18 and 19). Scratches on the surface lead to a decreased initial contact angle and higher contact line friction, whereas mechanical deformations of the foil such as wrinkles may cause local pinning effects. All of the mentioned irregularities will lead to shape deviations of the liquid lens during operation which cause aberrations of the wavefront. However, as most of them are introduced during fabrication and assembly, their influence is time-invariant and can thus be compensated for by calibration prior to operation.

3 Method

We now turn to the calibration method and the process for obtaining feedback on lens shape. As the lens cavity is completely sealed and its surface is inaccessible for mechanical measurements, optical characterization of its shape is used. To measure the surface profile, the transmitted wavefront of the device is recorded from which the surface shape is reconstructed. Figure 2(a) shows the calibration setup. A collimated laser is directed through the liquid lens and imaged onto a

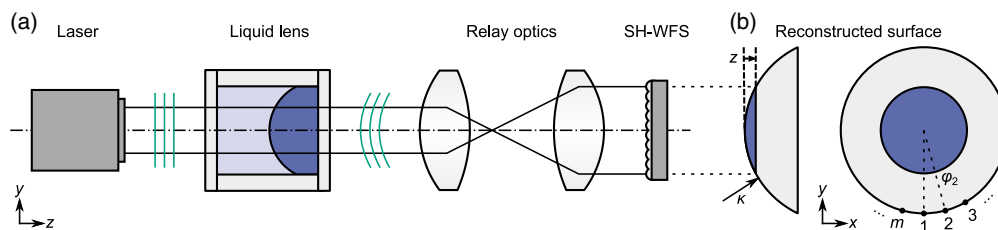


Fig. 2 (a) Measurement setup used to calibrate the tunable microlens. The transmitted wavefront of a collimated laser source is relayed onto a SH-WFS. (b) Surface profile that is reconstructed from the measured WFS data (blue) and remaining surface extrapolation by assuming constant curvature κ (white). Electrode center positions for a device with m electrodes are marked with black dots.

Shack–Hartmann wavefront sensor (SH-WFS) (WFS40-7AR, Thorlabs, Bergkirchen, Germany) by a relay system with a magnification of 2.

Figure 2(b) shows a schematic of the surface reconstruction from the wavefront data. Note that only a central portion of the liquid interface is illuminated and can thus be directly reconstructed (blue area). The illuminated area should generally be as large as possible to obtain the best correction result. For the results presented here, this area has a diameter of 3 mm whereas the inner diameter of the cavity is 5 mm. However, as surface tension is the defining mechanism for the shape of a liquid surface (in the absence of any external forces such as gravity, which is the case here), for spherical or toroidal shapes, the curvature κ is constant along any given section through the center of the surface. As a result, the shape of the entire interface (contact to contact) can be extrapolated from knowledge of the shape of the center region. Thus, if the illuminated area is defined as a spherical shape by adjusting the voltages at the contacts, it is valid to assume that the entire cross-section is therefore spherical.

A selection of different spherical surfaces within the desired operating region of the lens serves as test data for the calibration. The generation of these surfaces is achieved by controlling the surface height along the perimeter of the measured region. For an ideally spherical surface, the meniscus height at the perimeter, z , is constant along the circumference, and the curvature is then readily deduced from the height of the measured region. As the wavefront sensor provides no information about the absolute height of the liquid surface, z is defined relative to the surface vertex along the optical axis [see Fig. 2(b)]. There are m electrodes, and the angular position φ_i of each electrode i is known in relation to the measured wavefront as shown on the right in Fig. 2(b).

The difference between the target height (w_i) and the actual height (z_i) of the meniscus at each electrode position then leads to an optimization problem. Generally, the system should be considered a nonlinear multiple-input multiple-output system where a set of m voltage signals produces a change in the state of m height values. The voltage applied to a single electrode does affect the height at all positions, but not equally. Naturally, the height at any given electrode is most strongly linked to the voltage applied to itself. Therefore, the following assumption is made: the height of the liquid meniscus at each electrode is only controlled by the voltage applied to the corresponding electrode. This assumption enables the control structure to be made considerably simpler.

Figure 3 shows a schematic of the employed control structure. Quantities are expressed as matrices or vectors, \mathbf{w} , for example, is a vector of length m containing all individual w_i values, i.e., $\mathbf{w} = (w_1, \dots, w_m)^T$. The structure is based on a regular multi-variable integral controller with two notable differences that will be explained in this section.

The first difference is due to the assumption that the effect of each electrode is independent from all the others. For that reason, the controller gain matrix \mathbf{K} is a diagonal matrix of size $m \times m$ in which a single term is assigned to each electrode i . All other off-diagonal entries that would govern the interaction among electrodes are set to zero, effectively decoupling the electrodes from each other.

To further improve stability and minimize the remaining coupling effects among electrodes, only a subset of the control terms are updated in each cycle. This selection is the second difference to a standard controller and is done using the diagonal matrix \mathbf{D} . Which control terms are

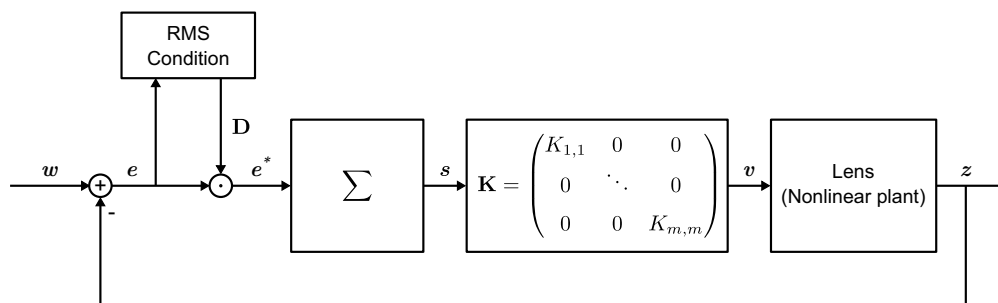


Fig. 3 Block diagram of the whole control system including the adaptive update condition, error sum, and controller gain \mathbf{K} . Capital boldface quantities are matrices, and lowercase bold quantities are vectors.

updated is determined in each cycle based on the global errors. Control terms whose error is greater than the root mean square (RMS) error of all electrodes receive an update, whereas others do not. Mathematically, their current error $e_{i,k}$ is simply set to zero which retains the error sum but leads to no change of the respective output voltage v_i . In this way, only the voltages of electrodes that contribute most to the shape deviation are adjusted.

At the beginning of the calibration procedure, the values of w are determined for a given spherical test shape from the geometry of an ideal spherical cap with a specified radius of curvature; for a spherical shape, all the w_i are the same for all i . The following calculation steps are then carried out in each iteration. First, the vector of error terms e_k is calculated as

$$e_k = w - z_k, \quad (1)$$

where w is the setpoint, and $z = (z_1, \dots, z_i)^T$ is a vector of the reconstructed heights at the electrodes at the current iteration k . These errors are then used to calculate the overall RMS error which is the basis for selecting the control terms to be updated. The elements of the $m \times m$ diagonal matrix D are constructed according to the rule

$$D_{i,j,k} = \begin{cases} 1, & \text{if } i = j \text{ and } |e_i| > \sqrt{\frac{1}{m} \sum_{i=1}^m e_i^2} \\ 0, & \text{otherwise} \end{cases} \quad (2)$$

Thus, only if the absolute error at electrode i is larger than the overall RMS value is $D_{i,j,k} = 1$ and the corresponding error is considered during the controller update. The selected error vector e_k^* is then given by

$$e_k^* = D e_k. \quad (3)$$

The controller update rule which receives e_k^* as an input consists of two parts. A sum $s_k = (s_{1,k}, \dots, s_{i,k})^T$ keeps track of cumulative errors for each electrode. It corresponds to the integral utilized in conventional I -controllers. Updates to the current sum are done by calculating

$$s_k = s_{k-1} + e_k^*. \quad (4)$$

Due to the selection of e_k^* , $e_i^* = e_i$ is only the case if the absolute error at electrode i is larger than the overall RMS value, and only then is the sum updated; otherwise, $e_i^* = 0$ and thus $s_{i,k} = s_{i,k-1}$, i.e., the value stays the same as in the previous iteration. The second part is the calculation of actuation voltages $v_k = (v_{1,k}, \dots, v_{i,k})^T$. They are determined as

$$v_k = K s_k, \quad (5)$$

where K is a $m \times m$ diagonal matrix with the individual gain values K_i . This step leads to decoupling because the voltage for each electrode only results from their respective error and not that of other electrodes. Interrelations among electrodes are thus disregarded.

Figure 4 demonstrates the method using a simulated example that combines tilt, varying dielectric thickness, and changes in initial contact angle. First, the target meniscus height for the desired curvature is calculated (black line). Then, an initial voltage is calculated using a measured contact angle curve and the voltages are applied. At the start of each cycle, the surface is measured and its profile is reconstructed. From the surface, the height along a circular region around the center is extracted and the heights at each electrode center position are determined as shown in Figs. 4(a) and 4(b). The difference between the measured and target height at each electrode is the error values for the individual controllers. To determine which controllers are updated in the current cycle, the RMS value of all errors is calculated (gray area). Controllers whose error value is larger than the RMS receive a controller update (filled blue markers) which changes the voltage for the next cycle. In the given example, the height at electrodes 9 to 18 is outside of the corridor which causes the voltages to be raised as shown in Fig. 4(c).

Each cycle, as the surface gets closer to the target and the RMS error decreases, previously unconsidered electrodes will fall outside of the corridor and also be adjusted. In this way, all electrodes that contribute to the mismatch between the measured and desired surface will eventually be considered if the algorithm is allowed to run for a sufficient length of time. Figure 4(d) shows the decrease in surface deviation over the whole device with the number of iterations. In practice, the algorithm is stopped once an acceptable RMS error is reached.

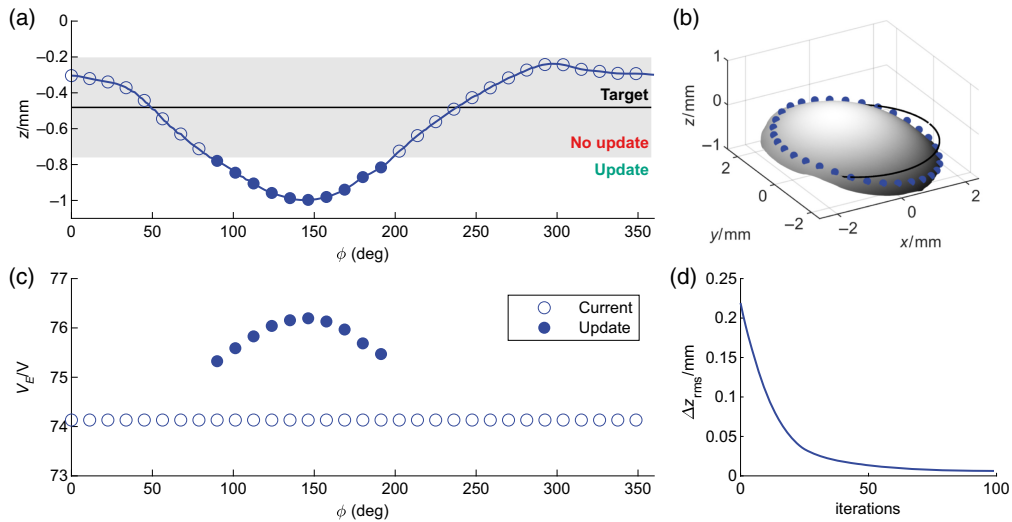


Fig. 4 (a) Simulated height along the circumference of the circular area; values at electrode positions are marked. (b) Example surface with target height (black) and measured height prior to optimization. (c) Voltages applied to each electrode before and after one cycle. (d) RMS deviation of the whole interface from the target surface shown over 100 iterations.

4 Simulation

To assess the method's performance, it was first tested in a simulation environment with commonly encountered defects, namely, tilt, dielectric thickness variations, and decreased initial contact angle. Here, the behavior of the liquid surface is replicated using the simulation tool Surface Evolver.²⁰ Given a set of geometry and contact angle constraints, it calculates the static equilibrium surface by energy minimization. To generate the contact angles, the simulation uses the ideal Young–Lippman equation as shown in Fig. 1(e).

First, a target surface is defined—in this case, a convex shape with a radius of curvature of $R_x = R_y = 5.5$ mm. The initial voltage is determined using this curvature according to ideal device behavior without defects. Then, parameters of the device such as the initial contact angle are deliberately modified to produce deviations from the desired contact angle. Surface Evolver computes the resulting surface profile which is used as an input to the calibration algorithm. The updated voltages in turn are used to calculate the contact angles for the next iteration and the calibration cycle continues for a fixed number of iterations.

The first defect that was simulated is a variation of the initial contact angle of a single electrode. Defects such as the one shown in Fig. 5(a) arise when the smooth hydrophobic surface

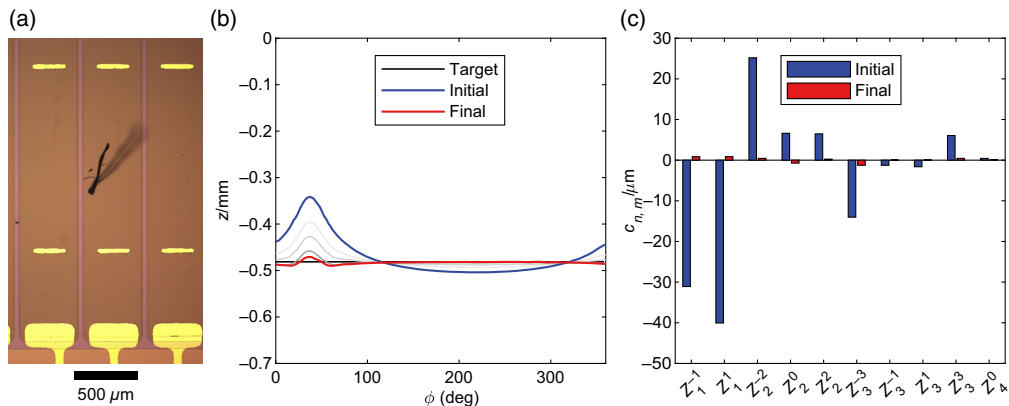


Fig. 5 (a) Mechanical defect of the hydrophobic coating as a result of handling errors. (b) Simulated height profiles along the circumference before and after calibration. (c) Shape deviation from ideal spherical shape expressed as Zernike coefficients before and after calibration.

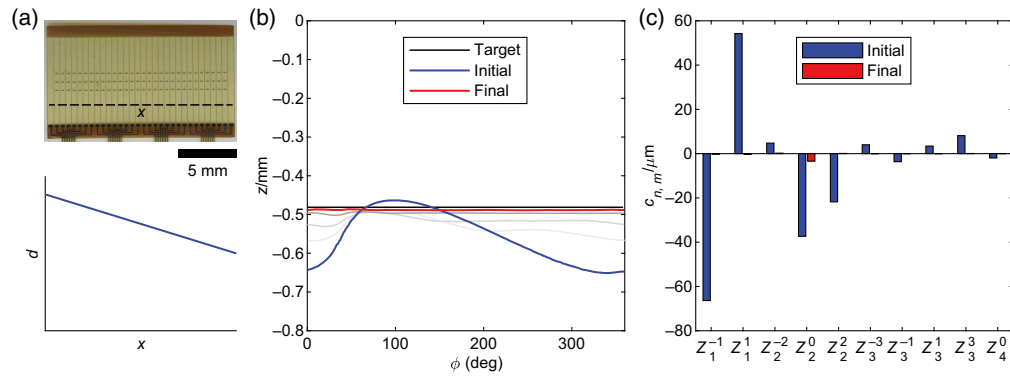


Fig. 6 (a) Linear variation in dielectric thickness along the length of the foil. (b) Simulated height profiles along the circumference before and after calibration. (c) Shape deviation from ideal spherical shape expressed as Zernike coefficients before and after calibration.

coating of the foil is damaged during handling or assembly. In the model, the initial contact angle of one electrode was reduced to 140 deg, whereas the rest was kept at 164.9 deg. The result is a peak-like elevation at the electrode position and a lower height outside of its vicinity. The deviations manifest themselves mainly as tilt, astigmatism, and trefoil. As demonstrated in Figs. 5(b) and 5(c), they are greatly reduced after 100 iterations with the RMS error decreasing from 37.7 to 3.4 μm .

Figure 6 shows the simulation results for a varying dielectric thickness. A linear change across the length of the foil was modeled with the end points corresponding to the two fitted measurements in Fig. 1(e). Once the foil is rolled up and inserted into the cavity, this type of defect will lead to a step-like change in electrowetting behavior where the foil ends meet. The result is a gradually changing height along the circumference with a drastic change at the position of the step. Again, tilt has the largest contribution to the deviation, followed by defocus and astigmatism. After calibration, the RMS error of the whole surface was decreased from 81.7 to 5.6 μm .

Tilt errors can occur during assembly of the lens when gluing the cavity onto the glass substrate as seen in Fig. 7(a), or they can result from mechanical tolerances of the lens mount. This defect was modeled by rotating the whole surface around the x -axis by 15 deg. The height profile consequently shows a characteristic sinusoidal shape and the deviations are dominated by the tilt coefficient. A large initial RMS error of 374 μm was decreased to 8.0 μm after the optimization.

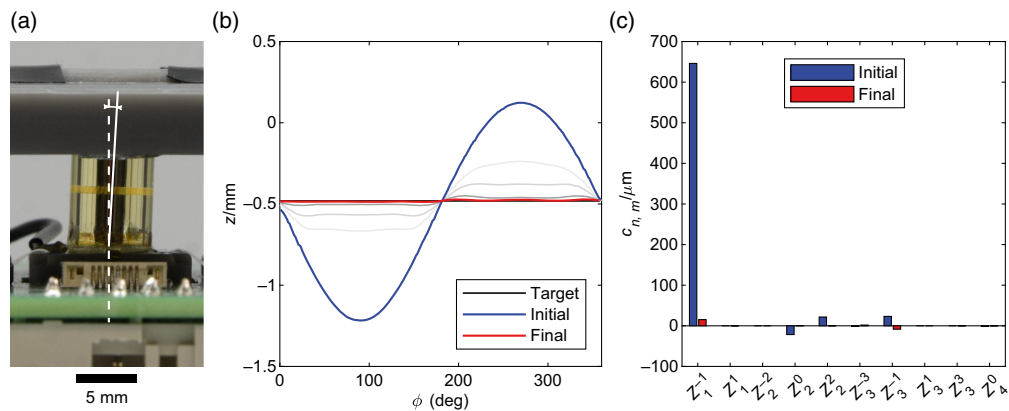


Fig. 7 (a) Tilt of the whole lens as a result of errors during assembly. (b) Simulated height profiles along the circumference before and after calibration. (c) Shape deviation from ideal spherical shape expressed as Zernike coefficients before and after calibration.

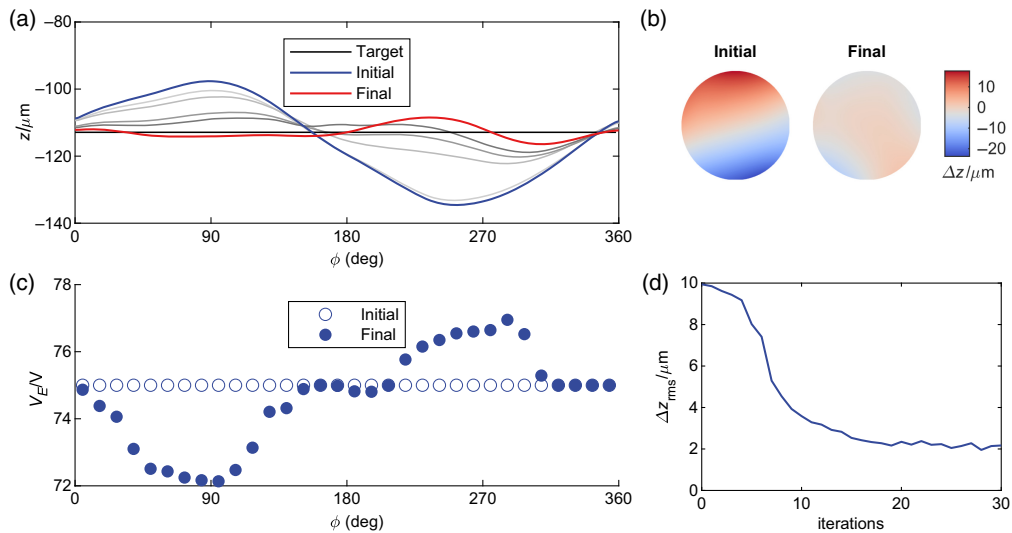


Fig. 8 (a) Measured height profiles along the circumference of the illuminated region before and after calibration. (b) Surface deviation from the ideal before and after calibration. (c) Determined actuation voltages. (d) RMS deviation of the whole illuminated interface from the target surface shown over 30 iterations.

5 Measurement

In addition to the simulations, the method was tested experimentally using a microlens of the type shown in Fig. 1(b). The lens was inserted into the setup as shown in Fig. 2(a), and the calibration algorithm was allowed to run for a fixed number of 30 iterations. The targeted operating point was a radius of $R_x = R_y = 9.2$ mm expected at an actuation voltage of 75 V. To ensure a static interface in each cycle, a wait time of 5 s is included which is well beyond the typical response time of our lens.

Figure 8 shows the results for the real device. As seen in Figs. 8(a) and 8(b), the main contribution to the mismatch was tilt. The overall deviation could be reduced effectively with some residual waviness remaining. Similar to the simulations, the RMS error decreases rapidly until it tends to an end value. The initial RMS error of $9.94 \mu\text{m}$ was decreased to $2.17 \mu\text{m}$ after the optimization. After calibration, the adjusted voltages resembled the inverse of the height profile with some small variations, hinting at local defects.

6 Operation

The measurement described in Sec. 5 only constitutes a single data point. For operation, the tunable lens is supposed to work in a specified power range, defined by the intended application. For that reason, the procedure has to be repeated a number of times across the desired range. Although it is possible to simply correct the contact angle relation shown in Fig. 1(e) using two data points, there might also be changes in electrowetting behavior along the height of the electrode. To take these changes into account, a larger number of samples is required. The resulting data include localized variations in actuation behavior on a per-electrode basis, thus enabling operation using interpolation or a lookup table. If desired, the voltage-to-contact angle relation inside the device could even be reconstructed on a per-electrode basis.

Although the simulations can be run until full convergence is reached, in practice, there needs to be a defined criterion. This is either a fixed number of iterations or a corridor around the target that is acceptable for the application at hand. An intrinsic criterion is the repeatability of the device itself. Once the deviation around the target is in a comparable range to the expected variation for repeated recreations of the same operating point, further continuing optimization is ineffective.

The time required to perform a complete calibration depends heavily on the device used and the intended application. For example, an imaging application that calls for the best shape fidelity

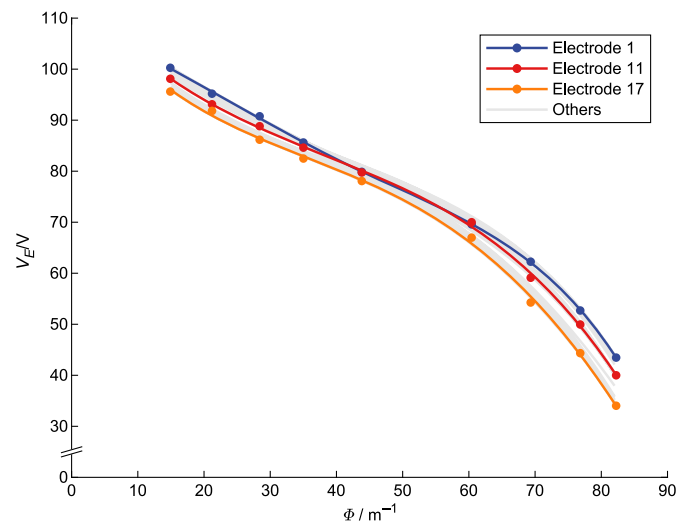


Fig. 9 Example interpolation curves for three example electrodes in a 32-electrode device. Points represent data obtained from calibration and lines are polynomial fits of fourth order. Gray lines show the remaining electrodes.

possible will require a higher number of calibration points across the operating range, increasing the total number of iterations performed.

The time for a single iteration, however, is mostly determined by the characteristics of the device, rather than the processing time. To ensure a proper initial state before actuation and a properly settled interface after applying the voltage, we included a wait time of 5 s each. This time interval is roughly equivalent to 20 times the step response of the system and is thus chosen very conservatively.²¹ In comparison, the measurement and computing time are relatively brief, at ~ 1 s combined, allowing the processing to take place during the off-interval. A single iteration of the algorithm thus takes 10 s and an optimization run of 30 iterations requires 5 min. However, this time can be reduced considerably if the wait time is adjusted to the minimal value that produces reliable results for the dynamics of the given lens.

Figure 9 gives an example of a completed lens calibration. In this case, the calibration was performed in the range between 15 and 82 diopters with nine individual steps. For each step, the algorithm was run for 50 iterations. The figure shows data for 3 of the 32 electrodes as well as corresponding fourth-order polynomial fits. This specific set of examples was chosen because it illustrates different deviations, namely offset and linearity error. Although the overall shape of the curves looks similar, there are evident differences in slope and offset. The maximum deviation of 9.4 V was observed between electrode 1 and electrode 17. Electrode 17 shows similar behavior to the other two but with an offset in voltage, that is, it is on average 5.1 V lower than electrode 1. When comparing electrodes 1 and 11, a close match is seen in the central region of the operating range with the two curves deviating again toward the ends, indicating a change in actuation behavior along the height of the electrode. Given the variations present in the calibration curves, a shape error equivalent of several diopters is expected for the uncalibrated device.

7 Conclusion

In conclusion, we have demonstrated how commonly encountered fabrication and assembly defects impact the shape fidelity of multi-electrode electrowetting lenses. Further, we have shown through simulation and measurement that our calibration method effectively reduces shape deviations that arise from such defects. For the utilized real microlens, the RMS error was reduced to 22% of its original value. The method presented here describes an inexpensive, fully automatic, easy-to-implement way of calibrating microlenses with a high number of actuators.

Disclosures

The authors declare that they have no conflicts of interest.

Code and Data Availability

The data that support the findings of this study are available from the corresponding author, DS, upon reasonable request.

Acknowledgments

The authors gratefully acknowledge Marcel Steidle for the helpful discussions on the topic.

References

1. S. Kuiper and B. H. W. Hendriks, "Variable-focus liquid lens for miniature cameras," *Appl. Phys. Lett.* **85**, 1128–1130 (2004).
2. K. Mishra, A. Narayanan, and F. Mugele, "Design and wavefront characterization of an electrically tunable aspherical optofluidic lens," *Opt. Express* **27**, 17601 (2019).
3. J. Cheng and C.-L. Chen, "Adaptive beam tracking and steering via electrowetting-controlled liquid prism," *Appl. Phys. Lett.* **99**, 191108 (2011).
4. J.-B. Xu et al., "Electrowetting liquid lens integrating adaptive liquid iris," *Opt. Laser Technol.* **169**, 110023 (2024).
5. D. Wang et al., "Design and fabrication of a focus-tunable liquid cylindrical lens based on electrowetting," *Opt. Express* **30**, 47430–47439 (2022).
6. B. Liu et al., "Underwater hyperspectral imaging system with liquid lenses," *Remote Sens.* **15**, 544 (2023).
7. R. Oliva-García et al., "Monocular real time full resolution depth estimation arrangement with a tunable lens," *Appl. Sci.* **12**, 3141 (2022).
8. C. Liu et al., "Continuous optical zoom microscope with extended depth of field and 3D reconstruction," *PhotonIX* **3**, 20 (2022).
9. D. Kopp and H. Zappe, "Tubular astigmatism-tunable fluidic lens," *Opt. Lett.* **41**, 2735–2738 (2016).
10. P. Zhao, D. Sauter, and H. Zappe, "Tunable fluidic lens with a dynamic high-order aberration control," *Appl. Opt.* **60**, 5302–5311 (2021).
11. D. Sauter et al., "Simultaneous beam steering and shaping using a single-interface optofluidic component," *J. Opt. Microsyst.* **1**, 044002 (2021).
12. M. Bøgh Stokholm et al., "3D-imaging: a scanning light pattern projector," *Appl. Opt.* **55**, 9074 (2016).
13. B. de Boer et al., "Control of an electrowetting-based beam deflector," *J. Appl. Phys.* **107**, 063101 (2010).
14. W. Y. Lim et al., "Calibration and characteristics of an electrowetting laser scanner," *IEEE Sens. J.* **20**, 3496–3503 (2020).
15. D. Sauter and H. Zappe, "Closed-loop wavefront calibration of a multi-electrode electrowetting-based tunable microlens," *Proc. SPIE* **12899**, 1289903 (2024).
16. L. Bakule, "Decentralized control: an overview," *Annu. Rev. Control* **32**, 87–98 (2008).
17. H.-S. Ahn, Y. Chen, and K. L. Moore, "Iterative learning control: brief survey and categorization," *IEEE Trans. Syst. Man Cybern. Part C (Appl. Rev.)* **37**, 1099–1121 (2007).
18. D. Kopp et al., "Tubular optofluidics as a versatile optical toolbox," in *19th Int. Conf. Solid-State Sens. Actuat. Microsyst. (Transducers)*, pp. 866–869 (2017).
19. D. Kopp, T. Brender, and H. Zappe, "All-liquid dual-lens optofluidic zoom system," *Appl. Opt.* **56**, 3758–3763 (2017).
20. K. A. Brakke, "The surface evolver," *Exp. Math.* **1**, 141–165 (1992).
21. P. Zhao, Y. Li, and H. Zappe, "Accelerated electrowetting-based tunable fluidic lenses," *Opt. Express* **29**, 15733–15746 (2021).

Daniel Sauter received his BEng degree in mechatronics from the Baden-Wuerttemberg Cooperative State University Stuttgart in 2015 and his MSc degree in embedded systems engineering from the University of Freiburg in 2020. Currently, he is a PhD candidate at the Laboratory for Micro-Optics, and his research interests are focused on optofluidic devices and electrowetting.

Hans Zappe is a professor of micro-optics at the University of Freiburg in Germany. He earned his BSc and MSc degrees from MIT in 1983 and his PhD from the University of California, Berkeley, in 1989, all in electrical engineering. He served at IBM (United States), the Fraunhofer Institute for Applied Solid State Physics (Germany), and the Centre Suisse d'Electronique et de Microtechnique (Switzerland) before joining the Department of Microsystems Engineering at the University of Freiburg in 2000. He is a fellow of SPIE, OSA, and IOP and is the Editor-in-Chief of the *SPIE Journal of Optical Microsystems*.